

Title: Layer-by-layer epitaxial growth of perovskite heterostructures with tunable band offsets

Authors: Yang Lu^{1,2†}, Young-Kwang Jung^{1†}, Milos Dubajic¹, Xinjuan Li³, Shabnum Maqbool^{1,2}, Qichun Gu¹, Xinyu Bai², Yorrick Boeije^{1,2}, Xian Wei Chua^{1,2}, Alessandro J. Mirabelli^{1,2}, Taeheon Kang¹, Lars Sonneveld⁴, Youcheng Zhang², Thomas A. Selby¹, Capucine Mamak¹, Kan Tang⁵, Zhongzheng Yu², Tianjun Liu², Miguel Anaya¹, Stephen Barlow⁵, Seth R. Marder^{5,6}, Bruno Ehrler⁴, Caterina Ducati³, Richard H. Friend^{2*}, Samuel D. Stranks^{1,2*}

Affiliations:

¹ Department of Chemical Engineering and Biotechnology, University of Cambridge; Cambridge, CB3 0AS, UK

² Cavendish Laboratory, University of Cambridge; Cambridge, CB3 0HE, UK

³ Department of Materials Science and Metallurgy, University of Cambridge; Cambridge, CB3 0FS, UK

⁴ LMPV-Sustainable Energy Materials Department, AMOLF; Amsterdam, 1098 XG, The Netherlands

⁵ Renewable and Sustainable Energy Institute (RASEI), University of Colorado Boulder; Boulder, 80309, United States

⁶ Department of Chemistry and Department of Chemical and Biological Engineering, University of Colorado Boulder; Boulder, 80309, United States

†These authors contributed equally to this work.

*Corresponding author. Email: Richard H. Friend, rhf10@cam.ac.uk; Samuel D. Stranks, sds65@cam.ac.uk

Abstract: Halide perovskites exhibit superior optoelectronic properties but lack precise thickness and band offset control in heterojunctions, critical for modular multilayer architectures such as multiple quantum wells. We demonstrate vapor-phase layer-by-layer heteroepitaxial growth exemplified by CsPbBr₃ deposition on single crystals of PEA₂PbBr₄ (PEA: 2-phenylethylammonium). Angstrom-level thickness control and sub-Angstrom smooth layers enable quantum-confined photoluminescence of CsPbBr₃ from monolayer, bilayer, and through to bulk. The interfacial structure controls the electronic structure from Cs-PEA-terminated interface (type-II heterojunction) to PEA-PEA-terminated (type-I), with a layer-tunable band offset shift exceeding 0.5 electron volt. Electron transfer from CsPbBr₃ to PEA₂PbBr₄ for type-II Cs-PEA heterojunction results in delayed electron-hole recombination beyond 10 microseconds. Precise quantum confinement control and large band offset tunability unlock perovskite heterojunctions as platforms for scalable, superlattice-based optoelectronic applications.

Main Text:

The successful commercialization of III-V semiconductor technologies (1–3) has been driven by vapor-phase layer-by-layer (LbL) heteroepitaxy, which enables atomic-level control over material and interface quality. This level of precision has allowed engineering of critical parameters, including bandgap, band offset and layer thickness in multilayer heterostructures such as multi-quantum-wells (MQWs) that guide charge transport and recombination dynamics. Halide perovskites, which have the advantages of low-cost and low-temperature processability, have demonstrated competitive performance in multi-junction solar cells and light-emitting diodes (LEDs)(4–8), and also hold great promises for advanced heterostructure-based devices(9). However, precise control over band properties and thicknesses remains a major bottleneck. Unlike III-V semiconductors, where alloying and strain engineering enable precise nanoscale tuning of bandgaps and band alignment, these strategies are ineffective in three-dimensional (3D) perovskite heterojunctions due to the high halide ion mobility(10, 11).

Two-dimensional (2D) halide perovskites provide a viable route for heterojunction bandgap engineering. Their larger intrinsic bandgaps, self-terminating surfaces, strong lattice templating, and extensive tunability through the incorporation of a vast library of organic cations, make heterostructures formed by 2D and 3D perovskites promising for multilayer device engineering. Stacked 2D/3D layers have been explored as passivation layers for solar cells and as natural MQW structures in LEDs and lasing(12–22), but solution-processing methods with polar solvents leads to quasi-2D phase heterogeneity, interfaces lacking atomic-scale structure definition, and variations in layer thicknesses. Several strategies, including orthogonal solvent engineering(23–26) and formation of heteroepitaxy through two-stage nucleation(27–29) or self-assembly of nanocrystals(30, 31), have improved interfacial phase purity. However, these approaches still lack the capability to precisely control layer thickness in the sub-10-nanometer range uniformly over a large area(19, 32, 33), as well as to be extended to multilayer heterostructures(9) – both crucial for fabricating advanced devices. Vapor-phase heteroepitaxy has shown good thickness control for perovskites with other salts, though not achieving LbL growth (34). Without a method to achieve precise nanoscale band structure engineering on electronically active layers, perovskite-based multilayer heterostructure devices remain out of reach.

We report vapor-phase LbL heteroepitaxial growth of 3D perovskite CsPbBr₃ on 2D perovskite single crystals. The as-grown perovskite heterostructure not only ensures precise and uniform thickness control but also enables tunable band offsets, overcoming key limitations of solution-based synthesis. The structure of the atomically sharp and well-defined heterointerfaces was examined by x-ray crystallographic tools and atomical resolution electron microscopy. We combined computational simulations and optical spectroscopic measurements to show that large band offset shift could be achieved by precisely controlling the interfacial structure through tuning the deposition conditions, allowing either type-I or type-II heterojunctions and enabling tailored charge transport and recombination dynamics. The heteroepitaxial templating also enabled a reduction in defect densities, enhanced carrier transport, and higher photoluminescence quantum yields (PLQY) in the CsPbBr₃ layer.

Heteroepitaxy relation

We primarily focused on PEA₂PbBr₄ single crystals as the 2D perovskite substrate. The crystal plane of PEA₂PbBr₄ (space group: $P\bar{1}$) containing a, b axes ($\gamma \approx 90^\circ$) can align well with the pseudo-cubic CsPbBr₃ because of the matching network of [PbBr₆] octahedra at the interface (fig. S3)(28, 30). To fabricate the epitaxial heterostructure, the PEA₂PbBr₄ single crystal was freshly cleaved

to expose an atomically flat (002)_{2D} surface, as confirmed by atomic force microscopy (AFM) and X-ray diffraction (XRD) (fig. S1). The heteroepitaxial growth of CsPbBr₃ was achieved through thermal co-evaporation of CsBr and PbBr₂ in a multisource deposition chamber (Fig. 1A), with precise control over their relative deposition rate by a separate quartz crystal microbalance to ensure stoichiometric formation of CsPbBr₃. Deposition rates ranging from 0.2 Å/s to 2 Å/s gave similar structural properties (fig. S2). A high-angle annular dark-field scanning transmission electron microscopy (HAADF-STEM) cross-sectional image (Fig. 1A, top-right) shows a sharp interface across large areas and no sign of grain boundaries or dislocation lines.

We confirmed heteroepitaxial growth using two most representative planes from 3D reciprocal space from single-crystal XRD (Fig. 1, B to D). The experimental patterns matched simulated PEA₂PbBr₄ and CsPbBr₃ lattice overlaps (Fig. 1D). Details of refined unit cell parameters are summarized in Table S1. For the heterostructure, only a single additional set of CsPbBr₃ reflections was observed in the (0*kl*)_{2D} plane (Fig. 1C, top) (35), with no sign of polycrystallinity or alternative orientations, confirming single orientation heteroepitaxy. The pseudo-cubic nature of the CsPbBr₃ lattice indicated multiple possible orientations that would allow heteroepitaxy, but we could not precisely obtain their orientation relationships from the single crystal diffraction data, as seen in reciprocal space and in real space: the [002]_{3D} axis of orthorhombic CsPbBr₃ aligns normal to the 2D perovskite layers (the *c** axes of PEA₂PbBr₄ and CsPbBr₃ overlap in Fig. 1E), and in the interfacial plane, the [110]_{3D}/[1 $\bar{1}$ 0]_{3D} axis of the CsPbBr₃ overlaps with the [020]_{2D}/[200]_{2D} axis of the PEA₂PbBr₄ (Fig. 1F, fig. S3).

Since the Pb-plane spacing along the [002]_{3D} axis of CsPbBr₃ was slightly larger than that along the other two directions, this orientation provided the best lattice matching between the 3D and 2D perovskites in the interfacial plane. This is evident in the bottom panels in Fig. 1C, D, where the CsPbBr₃ lattice points in its (*hk*0)_{3D} plane overlap with the PEA₂PbBr₄ lattice points in its $\perp c^*_{2D}$ plane. The diffraction pattern of the [002]_{3D} axis could also be easily distinguished from that of the [110]_{3D}/[1 $\bar{1}$ 0]_{3D} axes in the heterostructure sample's (0*kl*)_{2D} and $\perp c^*_{2D}$ planes (Fig. 1C, and simulated CsPbBr₃ patterns in Fig. 1D and fig. S3). Although both planes belong to the main axis of the orthorhombic (*Pbnm a⁻a⁻c⁺*) CsPbBr₃, the [002]_{3D} axis featured an in-plane tilting of the octahedra, whereas the other two planes featured out-of-plane tilting(36).

Out-of-plane XRD patterns in Bragg-Brentano geometry (fig. S4) provided additional evidence for the highly selective [002]_{3D} orientation. For randomly oriented CsPbBr₃ deposited on glass, a double-peak appeared at 15.05° ([002]_{3D}) and 15.21° ([110]_{3D}/[1 $\bar{1}$ 0]_{3D}), consistent with an orthorhombic structure. By contrast, the heteroepitaxially grown CsPbBr₃ on the 2D perovskite crystal had a single, sharp peak at 15.05°, indicating that the [002]_{3D} axis alone aligns in the out-of-plane direction. Differentiating between the [110]_{3D} and [1 $\bar{1}$ 0]_{3D} axes was challenging because of their minimal *d*-spacing difference (around 0.1%, table S1). The highly selective orientation for the [002]_{3D} axis across the entire substrate, first observed for pseudo-cubic CsPbBr₃, demonstrated that the heteroepitaxy strictly regulated the CsPbBr₃ growth under preferred lattice matching, and promoted a highly ordered lattice structure.

The highly ordered lattice of CsPbBr₃ showed improved optical properties. Using photothermal deflection spectroscopy (PDS), we measured the optical absorption tail into the semiconductor gap to extract the Urbach energy, a measure of band edge energetic disorder. For 30 nm-thick CsPbBr₃, we observed a decrease in Urbach energy from 37 meV (randomly grown on quartz) to 22 meV (heteroepitaxially grown on 2D perovskite), indicating that the heteroepitaxial growth reduced static energetic disorder (fig. S5). This reduction in Urbach energy was associated with enhanced radiative recombination efficiency. To isolate the PLQY of CsPbBr₃, we used 450-nm excitation

to avoid exciting the 2D layer. Under these conditions, the PLQY increased two-fold, from 0.63% on glass to 1.28% on 2D (fig. S6).

We further studied the transport properties of photoexcited species in the film by exciting the sample from the 3D side at a fixed spot with a near-diffraction-limited 405-nm laser beam, and raster-scanning the detection path across the sample to track the expansion of the PL spatial profile over time as carriers diffuse (37). For a 300-nm-thick CsPbBr₃ film where absorption by the underlying 2D layer is negligible (<0.1%), the diffusion coefficient for the CsPbBr₃ deposited on glass was observed to be 0.15 cm²/s, whereas that for the heterostructure sample was 0.39 cm²/s (fig. S7), demonstrating the superior transport properties enabled by heteroepitaxial growth. Four-point probe conductivity measurements from a lateral CsPbBr₃ device with Au/MoO_x contact layers grown heteroepitaxially on 2D single crystals also demonstrated a 7-times enhancement in conductivity and 3 orders of magnitude reduction in contact resistance compared to that deposited on glass (fig. S8). The improved electrical transport properties are consistent with enhanced charge transport because of fewer grain boundaries and aligned surface termination.

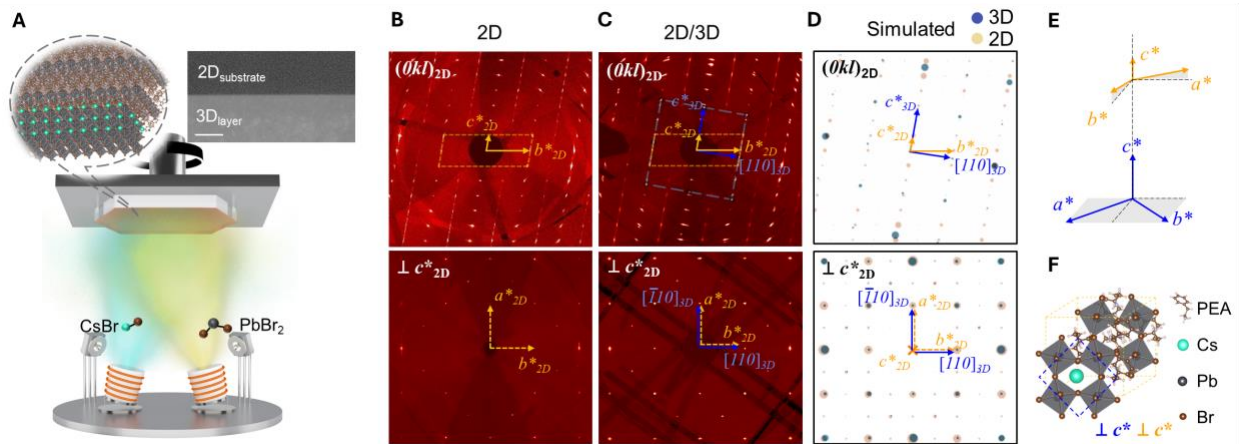


Fig. 1. Vapor-phase deposition realizes epitaxial CsPbBr₃-PEA₂PbBr₄ heterostructures. (A) Schematic illustration of vapor phase co-evaporation of CsPbBr₃ onto single crystal PEA₂PbBr₄ substrates. The top left inset shows a schematic illustration of heteroepitaxial CsPbBr₃-PEA₂PbBr₄ growth. The top right inset shows a HAADF-STEM image of a large-area atomically smooth and sharp heterointerface. Scale bar: 50 nm. (B-D) Measured $(0kl)_{2D}$ plane (top) and $\perp c^*_{2D}$ plane (bottom) of reciprocal space of (B) single crystal PEA₂PbBr₄, (C) heterostructure and (D) simulated heterostructure Bragg reflections. Thickness of CsPbBr₃ deposited was 500 nm. (E) Orientation relationship between heteroepitaxial CsPbBr₃ and PEA₂PbBr₄ in reciprocal space. (F) Atomic schematic illustration (top-view from $\perp c^*$) of CsPbBr₃-PEA₂PbBr₄ heterostructure.

Layer-by-layer growth

To understand the growth mode, especially at the heterointerface, we conducted a morphological study across a range of deposition thicknesses. Consistent LbL growth behavior (Fig. 2A) was observed among all thicknesses. As shown in Fig. 2B, AFM characterization of CsPbBr₃ grown on PEA₂PbBr₄ single crystals revealed ultrasmooth surfaces at nominal deposition thicknesses of 0.5, 5, 50 and 500 nm. The surfaces exhibited distinct island-like domains with consistent step heights of 0.6 nm, corresponding to exactly the size of the [PbBr₆] octahedral unit (Fig. 2D, also

see fig. S9 for varying stages in the LbL cycle and fig. S10 for larger areas). These observations confirmed LbL growth. Occasionally, at greater thickness up to 500 nm (Fig. 2B, right panel), multiple layers were observed, which is analogous to the LbL growth in III-V semiconductors where new layers may form near the completion of the previous layer(38).

5 The LbL growth on an cleaved single crystal surface led to the lowest reported root-mean-square (RMS) roughness of a metal halide perovskite thin-film to date. Statistical analyses across over 30 batches showed RMS roughness values consistently below 0.3 nm, or half of the thickness of one octahedral layer (fig. S11). This result is in stark contrast to CsPbBr₃ deposited on glass which showed RMS roughness of 4.01 nm from atomic force microscopy (AFM) (fig. S9), consistent
10 with roughness values reported for vapor-deposited 3D perovskite films(39, 40). Notably, regions between adlayers achieved roughness as low as 0.01 nm, indicating atomically smooth surfaces (Fig. 2C). We also note that the size of the adlayer islands may not directly reflect the nucleating density or island size during continuous deposition, as surface reconstruction can occur post-growth.

15 The LbL growth process, occurring one octahedral layer at a time, enabled conformal morphology (see fig. S12 for growth across steps) and precise thickness control across the whole substrate. This structure was also evidenced by Kiessig fringes from x-ray reflectivity (XRR) measurement (Fig. 2E) and Pendellösung fringes around the CsPbBr₃ (002) Bragg peaks (Fig. 2F). Fitting of the
20 Kiessig fringes showed the CsPbBr₃ had an expected thickness of 47 nm, as well as a roughness of 0.26 nm, which agreed with the AFM morphological results.

When the layers are only a few atoms thick, quantum-confined energy levels were reflected in their PL emission spectra. In Fig. 2G, at nominal deposition thicknesses of 0.6 nm (1L, red line), 1.2 nm (2L, blue line), and 2.4 nm (4L, green line), besides the main 2D substrate emission at 410 nm, an additional shoulder bump appears at 440, 468, and 500 nm, respectively. These emissions
25 from the top CsPbBr₃ layer reflected the strong 2D quantum confined nature as the energy closely matched their quasi-2D equivalents (PEA₂Cs_{n-1}Pb_nBr_{3n+1}) at n=2, n=3 and n=5 values(41, 42), though notably here the CsPbBr₃ layer was not sandwiched between the organic PEA cations from the cross-sectional STEM evidence shown in Fig. 3. At 10 nm thickness (Fig. 2G, yellow line), the emission shifted to 520 nm, corresponding to bulk CsPbBr₃. To further confirm that the
30 CsPbBr₃ top layer emission had uniform thickness, 440-nm excitation light was used and single emission peaks were observed for thickness of 1.2 nm (blue line), 2.4 nm (green line) and 10 nm (yellow line) (Fig. 2H).

We investigated the deposition of CsPbBr₃ on a series of other substrates. As shown above, deposition on glass shows random orientations and high roughness. Atomically flat single crystal
35 substrates with mismatched lattice symmetry, such as c-sapphire, do not support heteroepitaxial or LbL growth (fig. S13). By contrast, similar heteroepitaxial LbL growth was observed on BA₂PbBr₄ substrates, highlighting the generality of this approach across different 2D perovskites (fig. S14). We also investigated deposition of CsPbBr₃ on polycrystalline 2D perovskite films. In this case, the LbL growth mode was still observed. Grazing-incidence wide-angle x-ray scattering
40 (GIWAXS) patterns also revealed a highly oriented CsPbBr₃ with [002]_{3D} axis in the out-of-plane direction, well-matched in-plane lattices, and no detectable mixed-n phases (fig. S15). The absorption spectra further validated the absence of mixed-n phases (fig. S16). Similarly, electron backscatter diffraction (EBSD) characterization confirmed uniform out-of-plane orientations but random in-plane orientation (fig. S17, S18). Morphologically, the growth remained strongly
45 conformal, showing roughness levels nearly identical to the underlying templating polycrystalline 2D film (fig. S19). When only 1.2 nm and 2.4 nm CsPbBr₃ is deposited on poly-crystalline 2D

perovskite films, similar single emission peaks were observed as well, suggesting very uniform thickness (fig. S20). By contrast, deposition on glass showed bulk emission of CsPbBr₃ even when only nominally 1.2 or 2.4 nm was deposited (fig. S20). We note that no impurity phases from stoichiometric variations could be detected by X-ray diffraction when depositing on those various substrates (fig. S21).

We extended this polycrystalline system to several other 2D ligands cations including butylammonium, benzylammonium, 1-(2-naphthyl)methylammonium, 2-(thiophen-2-yl)ethylammonium. In each of these systems, the deposited CsPbBr₃ exhibited the characteristic highly oriented [002]_{3D} axis in the out-of-plane direction, and the absence of mixed-n phases from GIWAXS (fig. S22). The consistency of this templating growth across various ligands demonstrated the versatility of this vapor deposition method, making it a highly promising method for simple and scalable production. We focus the remainder of this study on the single crystal system with flat surfaces and no grain boundaries.

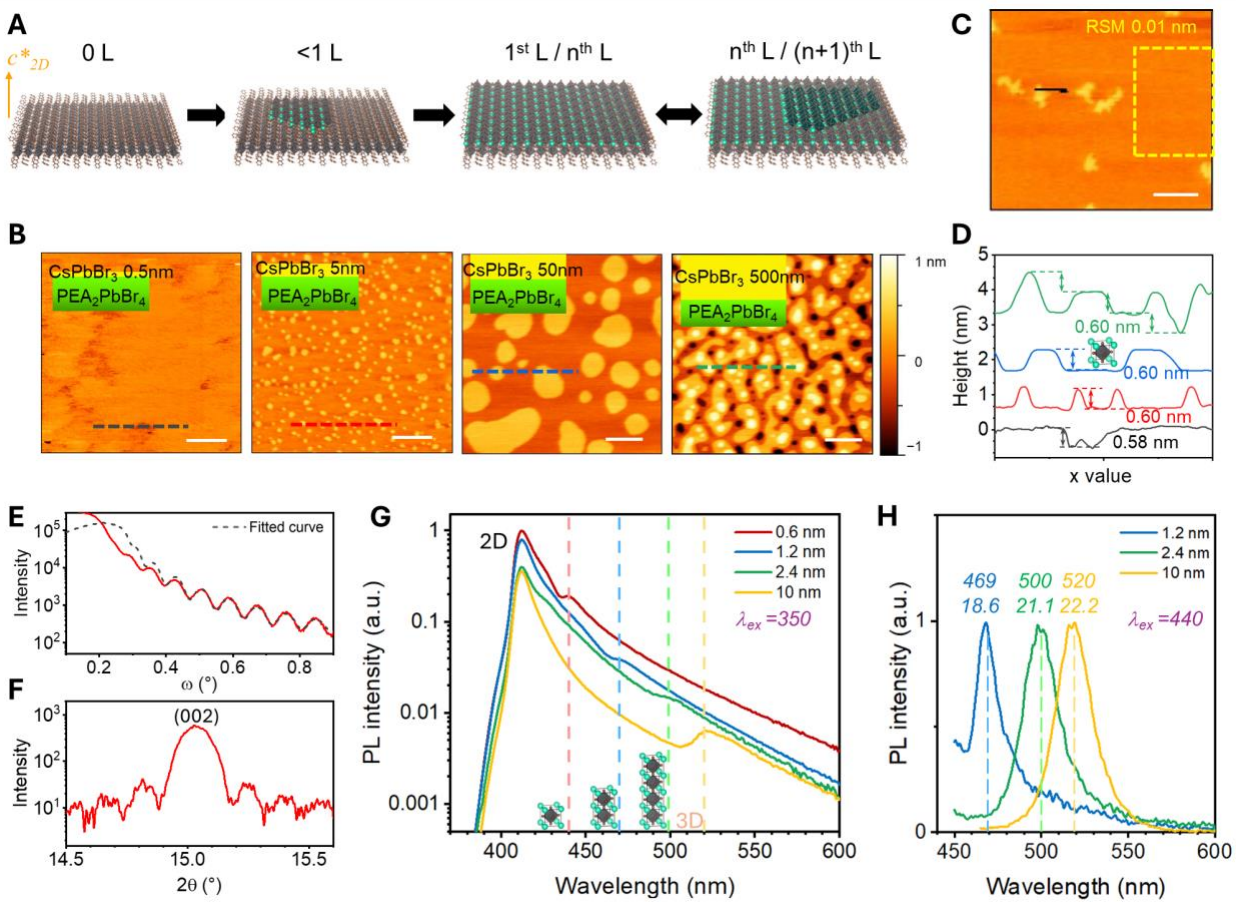


Fig. 2. Atomically smooth CsPbBr₃ fabricated by LbL growth. (A) Schematic illustration of LbL growth of CsPbBr₃ on PEA₂PbBr₄ (002)_{2D} surface. (B) Surface morphology study by AFM of LbL growth of CsPbBr₃ on single crystal PEA₂PbBr₄ from 0.5 nm (less than one Pb-Br octahedral layer), 5 nm, 50 nm until 500 nm. (C) RMS roughness of selected region of size 1 μm by 0.8 μm. Scale bars in (B) and (C): 400 nm. (D) Line profile of (B) showing clear steps corresponding to the Pb-Pb spacing in CsPbBr₃. (E) Kiessig fringes in XRR measurements of 50 nm CsPbBr₃ on PEA₂PbBr₄. (F) Pendellösung fringes around CsPbBr₃ (002) Bragg peak of 50 nm CsPbBr₃ on PEA₂PbBr₄. (G) Semi-log normalized PL emission spectra under 350 nm

excitation showing quantum confinement and uniform thickness from 0.6 (monolayer), 1.2 (bilayer), 2.4 (tetralayer) and 10 nm (the same as bulk). (H) Normalized PL emission spectra under 440 nm excitation showing single peak emission from 1.2 (bilayer), 2.4 (tetralayer) and 10 nm (the same as bulk). Text on top of peaks are fitted peak position and width in units of nanometers.

Tunable interfacial structures

The interfacial structure plays a pivotal role in determining heterojunction properties. A clean and sharp interface enables a pristine understanding of the electronic and optical behavior of the system. Cross-sectional atomic resolution HAADF-STEM imaging was used to determine the interfacial structure under different deposition conditions. When a stoichiometric ratio of CsBr and PbBr₂ was deposited on single crystal PEA₂PbBr₄ (Fig. 3A), clear crystal planes corresponding to Pb atom planes were observed, showing lattice spacing of 6.2 Å for the upper CsPbBr₃ and 17.0 Å for the bottom PEA₂PbBr₄, yielding an interfacial plane distance of 12.4 Å (Fig. 3C, left). By contrast, in Fig. 3B, co-sublimation with PEABr (CsBr:PbBr₂:PEABr = 1:1:0.1) resulted in an interfacial plane distance of 17.1 Å (Fig. 3C, right), whereas the 3D perovskite lattice structure as well as heteroepitaxial LbL growth remained unchanged (fig. S23–26). No quasi-2D phases were detected upon co-evaporating a small amount of PEABr from diffraction and PL (fig. S24). Energy-dispersive x-ray (EDX) mapping of Cs, Pb, Br, and C confirmed the presence of atomically sharp interfaces in both cases (selected region of Cs and C in Fig. 3A, B, and full map in fig. S27) and ruled out cation mixing during growth. After growth, the sharp interface showed promising stability with no signs of quasi-2D phases in XRD measurements after 6 months (fig. S28); even from very sensitive PL measurements, which will detect even trace amounts of lower bandgap phases due to energetic funneling of excited species, we do not observe any changes over weeks and only observe subtle hints of other phases even after 6 months (fig. S28). To study the pristine properties of the heterointerfaces in this work, samples were typically measured within one week. Transient absorption (TA) spectroscopy revealed that the energy transfer process from PEA₂PbBr₄ to CsPbBr₃ occurred within 2 to 3 ps for both heterostructures, versus 30 ps in solution-processed quasi-2D thin films (fig. S29)(30, 42–44). This acceleration suggested strong electronic coupling across the heterojunction without the presence of quasi-2D phases, facilitated by the clean and gap-free interface.

Based on the heteroepitaxial orientations, two possible interfacial structures could be expected: a Cs–PEA terminated interface (Fig. 3D, left), where the 2D perovskite is terminated by PEA ligands and the 3D perovskite is terminated by a Cs atom layer, and a PEA–PEA terminated interface (Fig. 3D, right), where both the 2D and 3D perovskites are terminated by PEA ligands. We performed density functional theory (DFT) calculations to determine the plane distances (fig. S30), and could attribute the distances in Fig. 3A to Cs–PEA-terminated interface (measured 12.4 Å vs calculated 12.9 Å) and in Fig. 3B to PEA–PEA-terminated interface (measured 17.1 Å vs calculated 16.7 Å). The simulated plane distances aligned well with the measured values, and corresponded to the deposition conditions: the presence of extra PEABr led to the PEA–PEA terminated interface. Our DFT calculations also revealed that formation of both Cs–PEA and PEA–PEA interfaces were energetically favorable, with interfacial binding energies of -10.94 and -8.32 meV/Å², respectively. Unlike solution processing, which typically only produces PEA–PEA-terminated interfaces because of the presence of excess PEA ligands(23, 28, 30), our vapor deposition method tuned the interfacial structure to atomic-level precision simply by adjusting deposition conditions.

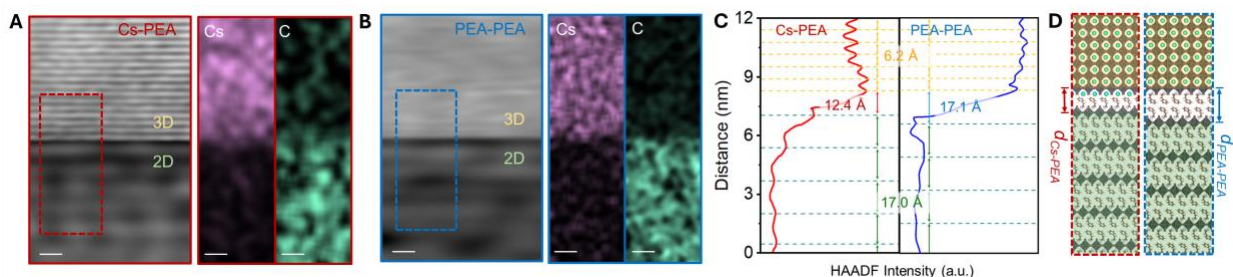


Fig. 3. Tuning interfacial structure of CsPbBr₃-PEA₂PbBr₄ heterostructure. (A) Left:

Atomic resolution HAADF-STEM image of Cs-PEA terminated CsPbBr₃-PEA₂PbBr₄ heterostructures. Right: EDX elemental mapping of Cs and C element at the Cs-PEA terminated interface. (B) Left: Atomic resolution HAADF-STEM image of PEA-PEA terminated CsPbBr₃-PEA₂PbBr₄ heterostructures. Right: EDX elemental mapping of Cs and C element at the PEA-PEA terminated interface. (C) Intensity profile extracted from rectangle boxes in (A, B), showing 6.2 Å inter-plane distance in CsPbBr₃ and 17.0 Å in PEA₂PbBr₄, and interface plane distance of 12.4 Å for Cs-PEA terminated and 17.1 Å for PEA-PEA terminated analogues. (D) Atomic schematics showing the interfacial structure of (left) Cs-PEA terminated interface and (right) PEA-PEA terminated interface. Scale bars: 2 nm.

We also used DFT to explore how the two different, well-defined interfacial structures influence electronic properties. Detailed partial density of states (PDOS) of Pb and Br atoms are shown in fig. S31. For the Cs-PEA and PEA-PEA interface, the DFT simulations predicted conduction band offset (CBO) values of -0.36 eV and 0.14 eV and showed a type-II and type-I band alignment, respectively (Fig. 4A, B). Such large shift of band offset up to 0.5 eV resulted from a combined contribution from surface dipole and interface bonding (fig. S32)(45, 46).

Figure 4C shows that on the CsPbBr₃ (001) surfaces with Cs termination, when the PEA⁺ ligands replace Cs⁺ ions, the oriented PEA⁺ ligands introduced an additional molecular dipole moment pointing toward vacuum. This dipole shifted the vacuum level upward by 0.55 V with respect to the macroscopic average of electrostatic potential, pushing the absolute electron energy levels deeper. By contrast, the contribution from interface bonding was relatively small. In the Cs-PEA interface, while the evident charge accumulation and depletion regions (Fig. 4D, top) suggested strong electronic interaction between Cs, Br ions on the surface of CsPbBr₃ and PEA ions on the surface of PEA₂PbBr₄, the planar-averaged charge density difference and electrostatic potential difference (Fig. 4D, bottom) exhibited a maximum amplitude of charge density fluctuation of 0.039 e/Å with a small built-in potential of 0.03 V. In the PEA-PEA interface, where weaker interactions between PEA ions on the two surfaces are observed (Fig. 4E, top), even lower maximum amplitude of charge density fluctuation (0.014 e/Å) was shown with a negligible built-in potential (Fig. 4E, bottom). The large shift of band offsets up to 0.5 eV induced by the molecular dipole is an advantage of these perovskites over III-V isovalent heterojunctions, where in the latter surface termination change shifts band offsets only by up to 0.1 eV, insufficient to switch between type-I and type-II band alignment(47).

The transition between type-I and type-II band alignment and its impact on carrier transfer pathways across interface was validated by studying the PL decay kinetics of the CsPbBr₃ (520 nm) and PEA₂PbBr₄ (415 nm) emissions from within the different heterojunctions under 400-nm

excitation using an intensified CCD (iCCD) camera with a time window up to 30 μs (Fig. 4F, G, and fig. S33), as well as directly probing carrier kinetics by TA spectroscopy (Fig. 4H and fig. S34) (23, 30). All samples featured a 30 nm CsPbBr₃ layer. Although structural characterization indicated no observable changes from PEABr co-evaporation (fig. S23-26), to minimize possible bulk passivation contributions from PEABr incorporation on PL decay kinetics (fig. S33), only the first 5 nm at the interface was modified, while the remaining 25 nm was identically deposited across samples. The two heterostructures with different interfaces were compared with the individual components as control samples (PEA₂PbBr₄ substrate, and CsPbBr₃ directly grown on glass).

In the type-I PEA–PEA-terminated heterostructure (Fig. 4F, blue line), the CsPbBr₃ PL decayed more slowly compared to the CsPbBr₃-only control (black line), possibly because of reduced nonradiative recombination for the CsPbBr₃ in the PEA–PEA heterostructure. After 1 μs (Fig. 4F), the decay trend resembled that of the CsPbBr₃ only control. TA measurements (Fig. 4H) show a slightly faster decay of PEA₂PbBr₄ bleach feature in the same time window, suggesting a transfer of excited species into the CsPbBr₃ layer (fig. S34).

In contrast, the type-II Cs–PEA-terminated heterostructure (red line) with photoinduced interfacial charge separation exhibited strong CsPbBr₃ PL quenching in the first 10 ns, followed by a slow, long-lived emission extending to beyond 10 μs . This charge separation behavior was further evidenced by its TA decay kinetics in the nanosecond range where both CsPbBr₃ (Fig. 4H) and PEA₂PbBr₄ (fig. S34) bleach features did not show substantial loss of carriers but instead showed a slower decay in the first 10 ns, indicating the charge carriers separated across the interface rather than through non-radiative recombination (48). At 10 ns in the TA data, the excited-state population in CsPbBr₃ within the type-II heterostructure remained above 40%, compared to below 5% in pure CsPbBr₃ or in the type-I heterostructure, suggesting that a substantial fraction of carriers had separated. This complementary information from TA and TRPL reveals that the band offset dominates carrier transfer pathways across the perovskite heterointerface in the first 10 ns, which can lead to long-lasting effects to 10 μs and beyond. Figure 4G further shows the integrated PL counts out to 30 μs , where we found 13% of the total carrier recombination in the Cs–PEA heterostructure occurred after 1 μs , compared to the PEA–PEA heterostructure where only 2% recombines after 1 μs . The lower total PL in the Cs–PEA heterostructure also suggested that the separated electron-hole pairs had a lower radiative recombination efficiency. Consistently, the PEA₂PbBr₄ emission at 415 nm exhibited a long-lived decay process only in the Cs–PEA heterostructure, but not for the PEA–PEA heterostructure (fig. S33). We also investigated the PL decay kinetics upon 450 nm excitation which excited only the CsPbBr₃ layer, and a faster decay was observed only in the Cs–PEA sample (fig. S35), again consistent with a type-II heterojunction.

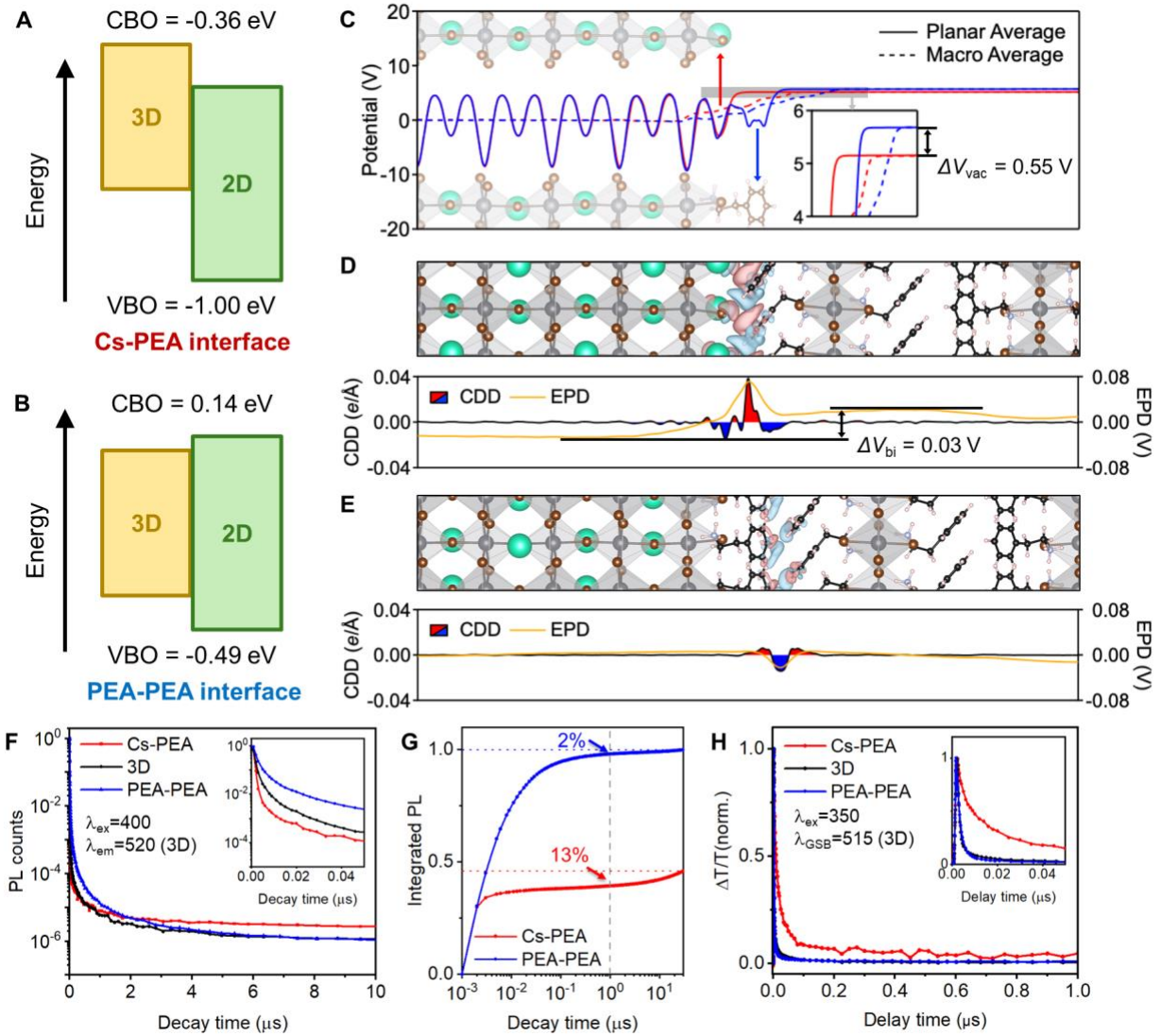


Fig. 4. Electronic and band alignment tunability of the CsPbBr₃-PEA₂PbBr₄ heterostructure interfaces.

(A, B) Calculated band alignment of Cs-PEA and PEA-PEA interfaces. (C) Planar-averaged (solid lines) and macroscopic-averaged (dashed lines) electrostatic potential profiles for CsPbBr₃ (001) surfaces with Cs termination (red) and PEA termination (blue). The macroscopic-averaged electrostatic potential ($\bar{V}(z)$) was calculated from $\bar{V}(z) = \frac{1}{c_0} \int_{z-c_0/2}^{z+c_0/2} V(z) dz$ where c_0 is the lattice constant of CsPbBr₃ along the z direction and $V(z)$ is the planar-averaged electrostatic potential. ΔV_{vac} is the different in vacuum levels between the Cs terminated surface and PEA terminated surface. Inset: Zoomed-in view of electrostatic potential profiles near vacuum region. (D) Top: Visualization of charge density difference (CDD) with atomic structure of Cs-PEA interface slab model. Charge accumulation region and charge depletion region are represented as red and blue clouds, respectively. Bottom: Planar-averaged CDD and electrostatic potential difference (EPD) of Cs-PEA interface. ΔV_{bi} is the built-in potential measured from the electrostatic potential difference. (E) Top: Visualization of CDD with atomic structure of PEA-PEA interface slab model as calculated by DFT. Bottom:

Planar-averaged CCD and EPD of PEA–PEA interface. (F) Photoluminescence decay kinetics at 520 nm (i.e., emission from 3D component) of pure 3D, Cs–PEA and PEA–PEA heterojunctions excited at 400 nm, $0.69 \mu\text{J}/\text{cm}^2$. Inset: zoomed-in view of the early-time dynamics from 0 to 50 ns. (G) Photoluminescence total intensities time-traces from (F) of the 3D emission from Cs–PEA and PEA–PEA heterostructures. (H) ns-TA kinetics at 515 nm (3D perovskite GSB) excited at 355 nm, $10 \mu\text{J cm}^{-2}$. Inset: zoomed-in view of the early-time dynamics from 0 to 50 ns.

Discussion

This study demonstrated a scalable, solvent-free, and industrial-compatible LbL heteroepitaxial growth for halide perovskites, achieving III-V semiconductor-level precision while maintaining substrate at room temperature. The resulting $\text{CsPbBr}_3\text{-PEA}_2\text{PbBr}_4$ heterostructure exhibited angstrom-level precise and uniform layer thickness down to monolayer which is important for quantum-confined applications, and to our knowledge, such precise LbL growth has not been realized in perovskite-related heteroepitaxy(49). Moreover, facile control of the atomic-level structure definition at the heterointerface by growth conditions enables shifting band offsets exceeding 0.5 eV, influencing charge separation or energy transfer. This effect is not seen in III-V semiconductors, where surface termination engineering typically yields band offset shifts below 0.1 eV unless heterovalent junctions are introduced, often at the cost of increased defect densities from mismatched bonding(47). The organic-inorganic hybrid nature of the heterointerface between 2D and 3D perovskite allows for both band offset modulation and LbL heteroepitaxial templating, offering a compelling advantage for designing a library of advanced heterostructure devices with a wide range of tunability in junction properties.

Our results have demonstrated a platform for band offset and precise thickness engineering in halide perovskite heterostructures. The bilayer perovskite heterostructures could serve as building blocks for fabricating artificial MQWs and tailored heterostructures for applications including LEDs, lasers, photodetectors and quantum devices. We anticipate that LbL epitaxy can be extended to other halide systems as well, though for iodide perovskites further consideration for phase management is required to allow the desired phase formation under the growth conditions. Further studies on electrical transport properties may uncover emergent charge dynamics and quantum effects. By bridging between the structural precision of conventional heteroepitaxy and the versatile halide perovskites, this work opens up new possibilities for both fundamental research and a new generation of tailored, high-efficiency MQW- and superlattice-based devices with facile processing.

References

1. F. Capasso, Band-gap engineering: From physics and materials to new semiconductor devices. *Science* **235**, 172–176 (1987).
2. E. Istrate, E. H. Sargent, Photonic crystal heterostructures and interfaces. *Rev. Mod. Phys.* **78**, 455–481 (2006).
3. Z. I. Alferov, Nobel Lecture: The double heterostructure concept and its applications in physics, electronics, and technology. *Rev. Mod. Phys.* **73**, 767–782 (2001).

4. S. D. Stranks, H. J. Snaith, Metal-halide perovskites for photovoltaic and light-emitting devices. *Nat Nanotechnol* **10**, 391–402 (2015).
5. Z.-K. Tan, R. S. Moghaddam, M. L. Lai, P. Docampo, R. Higler, F. Deschler, M. Price, A. Sadhanala, L. M. Pazos, D. Credgington, F. Hanusch, T. Bein, H. J. Snaith, R. H. Friend, Bright light-emitting diodes based on organometal halide perovskite. *Nat. Nanotechnol.* **9**, 687–692 (2014).
10. S. Hu, J. Wang, P. Zhao, J. Pascual, J. Wang, F. Rombach, A. Dasgupta, W. Liu, M. A. Truong, H. Zhu, M. Kober-Czerny, J. N. Drysdale, J. A. Smith, Z. Yuan, G. J. W. Aalbers, N. R. M. Schipper, J. Yao, K. Nakano, S.-H. Turren-Cruz, A. Dallmann, M. G. Christoforo, J. M. Ball, D. P. McMeekin, K.-A. Zaininger, Z. Liu, N. K. Noel, K. Tajima, W. Chen, M. Ehara, R. A. J. Janssen, A. Wakamiya, H. J. Snaith, Steering perovskite precursor solutions for multijunction photovoltaics. *Nature*, 1–3 (2024).
15. M. Li, Y. Yang, Z. Kuang, C. Hao, S. Wang, F. Lu, Z. Liu, J. Liu, L. Zeng, Y. Cai, Y. Mao, J. Guo, H. Tian, G. Xing, Y. Cao, C. Ma, N. Wang, Q. Peng, L. Zhu, W. Huang, J. Wang, Acceleration of radiative recombination for efficient perovskite LEDs. *Nature* **630**, 631–635 (2024).
20. X.-K. Liu, W. Xu, S. Bai, Y. Jin, J. Wang, R. H. Friend, F. Gao, Metal halide perovskites for light-emitting diodes. *Nat. Mater.* **20**, 10–21 (2021).
25. L. R. W. White, F. U. Kosasih, M. P. Sherburne, N. Mathews, S. Mhaisalkar, A. Bruno, Perovskite multiple quantum well superlattices: Potentials and challenges. *ACS Energy Lett.* **9**, 835–842 (2024).
30. Y. Yuan, J. Huang, Ion migration in organometal trihalide perovskite and its impact on photovoltaic efficiency and stability. *Acc. Chem. Res.* **49**, 286–293 (2016).
35. M. Lai, A. Obliger, D. Lu, C. S. Kley, C. G. Bischak, Q. Kong, T. Lei, L. Dou, N. S. Ginsberg, D. T. Limmer, P. Yang, Intrinsic anion diffusivity in lead halide perovskites is facilitated by a soft lattice. *Proc. Natl. Acad. Sci.* **115**, 11929–11934 (2018).
40. H. Chen, S. Teale, B. Chen, Y. Hou, L. Grater, T. Zhu, K. Bertens, S. M. Park, H. R. Atapattu, Y. Gao, M. Wei, A. K. Johnston, Q. Zhou, K. Xu, D. Yu, C. Han, T. Cui, E. H. Jung, C. Zhou, W. Zhou, A. H. Proppe, S. Hoogland, F. Laquai, T. Filleter, K. R. Graham, Z. Ning, E. H. Sargent, Quantum-size-tuned heterostructures enable efficient and stable inverted perovskite solar cells. *Nat. Photonics* **16**, 352–358 (2022).
45. W. Feng, K. Lin, W. Li, X. Xiao, J. Lu, C. Yan, X. Liu, L. Xie, C. Tian, D. Wu, K. Wang, Z. Wei, Efficient all-inorganic perovskite light-emitting diodes enabled by manipulating the crystal orientation. *J. Mater. Chem. A* **9**, 11064–11072 (2021).
50. I. Metcalf, S. Sidhik, H. Zhang, A. Agrawal, J. Persaud, J. Hou, J. Even, A. D. Mohite, Synergy of 3D and 2D perovskites for durable, efficient solar cells and beyond. *Chem. Rev.* **123**, 9565–9652 (2023).
55. D. Ma, K. Lin, Y. Dong, H. Choubisa, A. H. Proppe, D. Wu, Y.-K. Wang, B. Chen, P. Li, J. Z. Fan, F. Yuan, A. Johnston, Y. Liu, Y. Kang, Z.-H. Lu, Z. Wei, E. H. Sargent, Distribution control enables efficient reduced-dimensional perovskite LEDs. *Nature* **599**, 594–598 (2021).
60. B. Zhao, S. Bai, V. Kim, R. Lamboll, R. Shivanna, F. Auras, J. M. Richter, L. Yang, L. Dai, M. Alsari, X.-J. She, L. Liang, J. Zhang, S. Lilliu, P. Gao, H. J. Snaith, J. Wang, N. C.

Greenham, R. H. Friend, D. Di, High-efficiency perovskite–polymer bulk heterostructure light-emitting diodes. *Nat. Photonics* **12**, 783–789 (2018).

17. L. Luo, H. Zeng, Z. Wang, M. Li, S. You, B. Chen, A. Maxwell, Q. An, L. Cui, D. Luo, J. Hu, S. Li, X. Cai, W. Li, L. Li, R. Guo, R. Huang, W. Liang, Z.-H. Lu, L. Mai, Y. Rong, E. H. Sargent, X. Li, Stabilization of 3D/2D perovskite heterostructures via inhibition of ion diffusion by cross-linked polymers for solar cells with improved performance. *Nat. Energy* **8**, 294–303 (2023).

18. S. Sidhik, I. Metcalf, W. Li, T. Kodalle, C. J. Dolan, M. Khalili, J. Hou, F. Mandani, A. Torma, H. Zhang, R. Garai, J. Persaud, A. Marciel, I. A. Muro Puente, G. N. M. Reddy, A. Balvanz, M. A. Alam, C. Katan, E. Tsai, D. Ginger, D. P. Fenning, M. G. Kanatzidis, C. M. Sutter-Fella, J. Even, A. D. Mohite, Two-dimensional perovskite templates for durable, efficient formamidinium perovskite solar cells. *Science* **384**, 1227–1235 (2024).

19. K. Datta, S. Kim, R. Li, D. K. LaFollette, J. Yang, C. A. R. Perini, J.-P. Correa-Baena, Nanometer control of Ruddlesden-Popper interlayers by thermal evaporation for efficient perovskite photovoltaics. *Adv. Mater.* **36**, 2404795 (2024).

20. S. M. Park, M. Wei, J. Xu, H. R. Atapattu, F. T. Eickemeyer, K. Darabi, L. Grater, Y. Yang, C. Liu, S. Teale, B. Chen, H. Chen, T. Wang, L. Zeng, A. Maxwell, Z. Wang, K. R. Rao, Z. Cai, S. M. Zakeeruddin, J. T. Pham, C. M. Risko, A. Amassian, M. G. Kanatzidis, K. R. Graham, M. Grätzel, E. H. Sargent, Engineering ligand reactivity enables high-temperature operation of stable perovskite solar cells. *Science* **381**, 209–215 (2023).

21. R. Azmi, D. S. Utomo, B. Vishal, S. Zhumagali, P. Dally, A. M. Risqi, A. Prasetio, E. Ugur, F. Cao, I. F. Imran, A. A. Said, A. R. Pininti, A. S. Subbiah, E. Aydin, C. Xiao, S. I. Seok, S. De Wolf, Double-side 2D/3D heterojunctions for inverted perovskite solar cells. *Nature* **628**, 93–98 (2024).

22. C. Qin, A. S. D. Sandanayaka, C. Zhao, T. Matsushima, D. Zhang, T. Fujihara, C. Adachi, Stable room-temperature continuous-wave lasing in quasi-2D perovskite films. *Nature* **585**, 53–57 (2020).

23. M.-Y. Kuo, N. Spitha, M. P. Hautzinger, P.-L. Hsieh, J. Li, D. Pan, Y. Zhao, L.-J. Chen, M. H. Huang, S. Jin, Y.-J. Hsu, J. C. Wright, Distinct carrier transport properties across horizontally vs vertically oriented heterostructures of 2D/3D perovskites. *J. Am. Chem. Soc.* **143**, 4969–4978 (2021).

24. Y. Chen, Y. Lei, Y. Li, Y. Yu, J. Cai, M.-H. Chiu, R. Rao, Y. Gu, C. Wang, W. Choi, H. Hu, C. Wang, Y. Li, J. Song, J. Zhang, B. Qi, M. Lin, Z. Zhang, A. E. Islam, B. Maruyama, S. Dayeh, L.-J. Li, K. Yang, Y.-H. Lo, S. Xu, Strain engineering and epitaxial stabilization of halide perovskites. *Nature* **577**, 209–215 (2020).

25. Y. Lei, Y. Li, C. Lu, Q. Yan, Y. Wu, F. Babbe, H. Gong, S. Zhang, J. Zhou, R. Wang, R. Zhang, Y. Chen, H. Tsai, Y. Gu, H. Hu, Y.-H. Lo, W. Nie, T. Lee, J. Luo, K. Yang, K.-I. Jang, S. Xu, Perovskite superlattices with efficient carrier dynamics. *Nature* **608**, 317–323 (2022).

26. S. Sidhik, Y. Wang, M. De Siena, R. Asadpour, A. J. Torma, T. Terlier, K. Ho, W. Li, A. B. Puthirath, X. Shuai, A. Agrawal, B. Traore, M. Jones, R. Giridharagopal, P. M. Ajayan, J. Strzalka, D. S. Ginger, C. Katan, M. A. Alam, J. Even, M. G. Kanatzidis, A. D. Mohite, Deterministic fabrication of 3D/2D perovskite bilayer stacks for durable and efficient solar cells. *Science* **377**, 1425–1430 (2022).

27. J.-W. Lee, S. Tan, T.-H. Han, R. Wang, L. Zhang, C. Park, M. Yoon, C. Choi, M. Xu, M. E. Liao, S.-J. Lee, S. Nuryyeva, C. Zhu, K. Huynh, M. S. Goorsky, Y. Huang, X. Pan, Y. Yang, Solid-phase hetero epitaxial growth of α -phase formamidinium perovskite. *Nat. Commun.* **11**, 5514 (2020).
- 5 28. H. Min, N. Wang, N. Chen, Y. Tong, Y. Wang, J. Wang, J. Liu, S. Wang, X. Wu, P. Yang, H. Shi, C. Zhuo, Q. Chen, J. Li, D. Zhang, X. Lu, C. Zhu, Q. Peng, L. Zhu, J. Chang, W. Huang, J. Wang, Spin coating epitaxial heterodimensional tin perovskites for light-emitting diodes. *Nat. Nanotechnol.* **19**, 632–637 (2024).
- 10 29. Y. Meng, Y. Wang, C. Liu, P. Yan, K. Sun, Y. Wang, R. Tian, R. Cao, J. Zhu, H. Do, J. Lu, Z. Ge, Epitaxial growth of α -FAPbI₃ at a well-matched heterointerface for efficient perovskite solar cells and solar modules. *Adv. Mater.* **36**, 2309208 (2024).
- 15 30. Z. Zhu, C. Zhu, L. Yang, Q. Chen, L. Zhang, J. Dai, J. Cao, S. Zeng, Z. Wang, Z. Wang, W. Zhang, J. Bao, L. Yang, Y. Yang, B. Chen, C. Yin, H. Chen, Y. Cao, H. Gu, J. Yan, N. Wang, G. Xing, H. Li, X. Wang, S. Li, Z. Liu, H. Zhang, L. Wang, X. Huang, W. Huang, Room-temperature epitaxial welding of 3D and 2D perovskites. *Nat. Mater.* **21**, 1042–1049 (2022).
31. K. Wei, T. Zhou, Y. Jiang, C. Sun, Y. Liu, S. Li, S. Liu, X. Fu, C. Hu, S. Tian, Y. Yang, X. Fu, N. AlMasoud, S. M. H. Qaid, M. K. Nazeeruddin, H.-Y. Hsu, W.-D. Li, J. T. Kim, R. Long, W. Zhang, J. Chen, M. Yuan, Perovskite heteroepitaxy for high-efficiency and stable pure-red LEDs. *Nature*, 1–8 (2025).
- 20 32. J. Y. Park, R. Song, J. Liang, L. Jin, K. Wang, S. Li, E. Shi, Y. Gao, M. Zeller, S. J. Teat, P. Guo, L. Huang, Y. S. Zhao, V. Blum, L. Dou, Thickness control of organic semiconductor-incorporated perovskites. *Nat. Chem.* **15**, 1745–1753 (2023).
- 25 33. Z. Xu, H. Xi, X. Sun, H. Liu, J. Liu, Y. Ba, D. Chen, G. Zhang, C. Zhang, X. Ma, Y. Hao, Highly stable and sensitive (PEA)₂PbBr₄/CsPbBr₃ single-crystal heterojunction X-ray detector with ultra-low detection limit. *Adv. Funct. Mater.* **34**, 2400817 (2024).
- 30 34. J. S. Solomon, T. Soto-Montero, Y. A. Birkhölzer, D. M. Cunha, W. Soltanpoor, M. Ledinský, N. Orlov, E. C. Garnett, N. Forero-Correa, S. E. Reyes-Lillo, T. B. Haward, J. R. S. Lilly, L. M. Herz, G. Koster, G. Rijnders, L. Leppert, M. Morales-Masis, Room-temperature epitaxy of α -CH₃NH₃PbI₃ halide perovskite by pulsed laser deposition. *Nat. Synth* **4**, 432–443 (2025).
- 35 35. K. Shibuya, M. Koshimizu, F. Nishikido, H. Saito, S. Kishimoto, Poly[bis(phenethyl-ammonium) [di-bromido-plumbate(II)]-di- μ -bromido]]. *Acta Crystallogr. Sect. E Struct. Rep. Online* **65**, m1323–m1324 (2009).
- 36 36. M. Rodová, J. Brožek, K. Knížek, K. Nitsch, Phase transitions in ternary caesium lead bromide. *J. Therm. Anal. Calorim.* **71**, 667–673 (2003).
- 37 37. G. M. Akselrod, F. Prins, L. V. Poulikakos, E. M. Y. Lee, M. C. Weidman, A. J. Mork, A. P. Willard, V. Bulović, W. A. Tisdale, Subdiffusive exciton transport in quantum dot solids. *Nano Lett.* **14**, 3556–3562 (2014).
- 40 38. S. V. Ghaisas, A. Madhukar, Role of surface molecular reactions in influencing the growth mechanism and the nature of nonequilibrium surfaces: A Monte Carlo study of molecular-beam epitaxy. *Phys. Rev. Lett.* **56**, 1066–1069 (1986).

39. M. Shin, H. Lee, Y. Sim, Y. Cho, K. Choi, B. Shin, Modulation of growth kinetics of vacuum-deposited CsPbBr₃ films for efficient light-emitting diodes. *ACS Appl. Mater. Interfaces* **12**, 1944–1952 (2020).
40. L. Song, L. Huang, Y. Liu, X. Guo, C. Geng, S. Xu, Y. Xia, Y. Zhang, N. Luan, Y. Hu, Efficient thermally evaporated perovskite light-emitting devices via a bilateral interface engineering strategy. *J. Phys. Chem. Lett.* **12**, 6165–6173 (2021).
41. X. Yang, X. Zhang, J. Deng, Z. Chu, Q. Jiang, J. Meng, P. Wang, L. Zhang, Z. Yin, J. You, Efficient green light-emitting diodes based on quasi-two-dimensional composition and phase engineered perovskite with surface passivation. *Nat. Commun.* **9**, 570 (2018).
42. L. N. Quan, Y. Zhao, F. P. García de Arquer, R. Sabatini, G. Walters, O. Voznyy, R. Comin, Y. Li, J. Z. Fan, H. Tan, J. Pan, M. Yuan, O. M. Bakr, Z. Lu, D. H. Kim, E. H. Sargent, Tailoring the energy landscape in quasi-2D halide perovskites enables efficient green-light emission. *Nano Lett.* **17**, 3701–3709 (2017).
43. Q. Shang, Y. Wang, Y. Zhong, Y. Mi, L. Qin, Y. Zhao, X. Qiu, X. Liu, Q. Zhang, Unveiling structurally engineered carrier dynamics in hybrid quasi-two-dimensional perovskite thin films toward controllable emission. *J. Phys. Chem. Lett.* **8**, 4431–4438 (2017).
44. Y. Jiang, J. Wei, M. Yuan, Energy-funneling process in quasi-2D perovskite light-emitting diodes. *J. Phys. Chem. Lett.* **12**, 2593–2606 (2021).
45. Y.-K. Jung, K. T. Butler, A. Walsh, Halide perovskite heteroepitaxy: Bond formation and carrier confinement at the PbS–CsPbBr₃ interface. *J. Phys. Chem. C* **121**, 27351–27356 (2017).
46. A. Mahata, E. Mosconi, D. Meggiolaro, F. De Angelis, Modulating band alignment in mixed dimensionality 3D/2D perovskites by surface termination ligand engineering. *Chem. Mater.* **32**, 105–113 (2020).
47. A. Franciosi, C. G. Van de Walle, Heterojunction band offset engineering. *Surf. Sci. Rep.* **25**, 1–140 (1996).
48. J. Liu, J. Leng, K. Wu, J. Zhang, S. Jin, Observation of internal photoinduced electron and hole separation in hybrid two-dimensional perovskite films. *J. Am. Chem. Soc.* **139**, 1432–1435 (2017).
49. L. Wang, I. King, P. Chen, M. Bates, R. R. Lunt, Epitaxial and quasiepitaxial growth of halide perovskites: New routes to high end optoelectronics. *APL Mater.* **8**, 100904 (2020).
50. T. Sheikh, A. Nag, Mn doping in centimeter-sized layered 2D butylammonium lead bromide (BA₂PbBr₄) single crystals and their optical properties. *J. Phys. Chem. C* **123**, 9420–9427 (2019).
51. W. Kohn, L. J. Sham, Self-consistent equations including exchange and correlation effects. *Phys. Rev.* **140**, A1133–A1138 (1965).
52. G. Kresse, J. Furthmüller, Efficient iterative schemes for ab initio total-energy calculations using a plane-wave basis set. *Phys. Rev. B* **54**, 11169–11186 (1996).
53. G. Kresse, J. Furthmüller, Efficiency of ab-initio total energy calculations for metals and semiconductors using a plane-wave basis set. *Comput. Mater. Sci.* **6**, 15–50 (1996).
54. G. Kresse, D. Joubert, From ultrasoft pseudopotentials to the projector augmented-wave method. *Phys. Rev. B* **59**, 1758–1775 (1999).

55. P. E. Blöchl, Projector augmented-wave method. *Phys. Rev. B* **50**, 17953–17979 (1994).
56. J. P. Perdew, K. Burke, M. Ernzerhof, Generalized gradient approximation made simple. *Phys. Rev. Lett.* **77**, 3865–3868 (1996).
57. S. Grimme, J. Antony, S. Ehrlich, H. Krieg, A consistent and accurate ab initio parametrization of density functional dispersion correction (DFT-D) for the 94 elements H-Pu. *J. Chem. Phys.* **132**, 154104 (2010).

Acknowledgments: We acknowledge Dr. Jonathan Rawle for support during experiments on the I07 beamline at Diamond Light Source. We thank Dr. Giulio I. Lampronti for help with XRR measurements. We thank Diamond Light Source for access and support in use of beamline I07 (proposal SI32266, SI38601, SI30043), beamline I19 (proposal number CY33123, CY36628) and beamline I15 (proposal number CY38508). This work was supported by the Henry Royce Institute for advanced materials through the Equipment Access Scheme enabling access to XPS Suite and Ambient Cluster Tool facilities at Cambridge; EPSRC (EP/R00661X/1) and Cambridge Royce facilities grant EP/P024947/1. Via our membership of the UK's HEC Materials Chemistry Consortium, which is funded by EPSRC (EP/X035859/1), this work used the ARCHER2 UK National Supercomputing Service (<http://www.archer2.ac.uk>). This work was supported by the Henry Royce Institute for advanced materials through the Equipment Access Scheme enabling access to the FIB and TEM at Cambridge; Cambridge Royce facilities grant CAM-YR8-UI-042-REAS. We acknowledge the support of the Wolfson Electron Microscopy Suite and use of the Thermo Fisher Spectra 300 TEM funded by EPSRC grant EP/R008779/1. B.E. is also affiliated with the University of Groningen via an honorary appointment at the Zernike Institute for Advanced Materials.

Funding:

Engineering and Physical Sciences Research Council EP/V06164X/1 (YL, RHF, SDS)
Royal Society and Tata Group UF150033, URF\R\221026 (SDS)
European Research Council grant VAPOURISE, 101169608 (SDS)
Simons Foundation Grant No. 601946 (RHF)
UKRI guarantee funding for Marie Skłodowska-Curie Actions Postdoctoral Fellowships 2021 (EP/X025756/1) (YKJ)
UKRI guarantee funding for Marie Skłodowska-Curie Actions Postdoctoral Fellowships 2022 (EP/Y024648/1) (MD)
Winton Programme for Physics of Sustainability (YB)
National Science Scholarship from Agency for Science, Technology and Research (A*STAR, Singapore) (XWC)
D.M.P. VFdS74 foundation (AJM)

Trinity-Henry Barlow Scholarship (TK)

Connected Electronics and Photonics CDT EP/S022139/1 (CM)

Dutch Research Council (NWO), Gatan (EDAX), Amsterdam Scientific Instruments (ASI) and CL Solutions (19459) (LS, BE)

5 European Union's Horizon 2020 research and innovation programme (No. 947221) (BE)

Engineering and Physical Sciences Research Council Nano Doctoral Training Centre, EP/S022953/1 (TAS)

Royal Academy of Engineering Research Fellowship programme (MA)

National Science Foundation ECCS-2141949 (KT, SB, SRM)

10 **Author contributions:**

Conceptualization: YL, RHF, SDS

Methodology: YL, YKJ, XL, MD, CM, RHF, SDS

Fabrication: YL, QG, XB, KT

Density functional theory calculation: YKJ

15 Cross-sectional preparation, imaging, and analysis: XL

Structural and morphological investigation: YL, MD, QG, AJM, TK, LS, TAS, MA

Structure data analysis: MD

Spectroscopic investigation and analysis: YL, MD, SM, XB, YB, XWC, CM, ZY, TL

Electrical property investigation: YZ

20 Visualization: YL, YKJ, XL, MD, RHF, SDS

Funding acquisition: RHF, SDS

Project administration: SDS, RHF

Supervision: SDS, RHF, CD, BE, SRM, SB

Writing – original draft: YL, RHF, SDS

25 **Competing interests:** S.D.S. is a co-founder of Swift Solar Inc and Clarity Sensors Limited.

Data and materials availability: All data needed to evaluate the conclusions in the paper are available in the main text or the supplementary materials.

Supplementary Materials

Materials and Methods

30 Figs. S1 to S35

Tables S1 to S2